JACS
JOURNAL OF THE AMERICAN CHEMICAL SOCIETY
Article
Cite This: J. Am. Chem. Soc. 2018, 140, 17968−17976
pubs.acs.org/JACS

Extraordinary Dielectric Properties at Heterojunctions of Amorphous Ferroelectrics

M. Helena Braga,*[,†,‡] Joana E. Oliveira,[‡] Tianhan Kai,[§] Andrew J. Murchison,[†] Allen J. Bard,[§] and John B. Goodenough*[,†]

[†]The Materials Institute, Department of Mechanical Engineering, The University of Texas at Austin, Austin, Texas 78712, United States

[‡]LAETA, Department of Engineering Physics, FEUP, University of Porto, 4200-465 Porto, Portugal

[§]Center for Electrochemistry, Department of Chemistry, The University of Texas at Austin, Austin, Texas 78712, United States

Supporting Information

ABSTRACT: Materials having a high dielectric constant are needed for a variety of electrical applications from transistors to capacitors. Ferroelectric amorphous-oxide (glass) alkali-ion electrolytes of composition $A_{2.99}Ba_{0.005}ClO$ (A = Li, Na) are shown by two different types of measurement and different consistent analyses to have extraordinarily high dielectric constants, varying from 10^9 at 25 °C to 10^{10} at 220 °C if the glass is properly conditioned. These anomalously high dielectric properties coexist with alkali-ion conductivities at 25 °C that are equivalent to those of the best organic-liquid electrolytes of a Li-ion cell, and cyclic voltammetry (CV) in a Au/glass electrolyte/Au cell is stable from −10 to +10 V. A model to interpret microscopically all the key features of the CV curves shows that the electric-double-layer capacitors that form at the gold/electrolyte interfaces in the Au/glass electrolyte/Au heterojunction reverse polarization at an applied voltage $V = \pm 2.1$ V, resulting in three almost equivalent discharging capacitances for a single physical capacitor from −10 to +10 V.

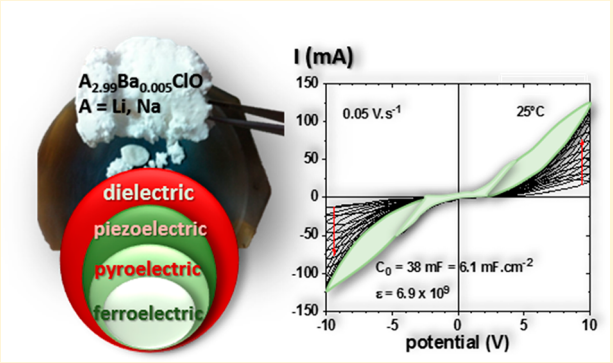

1. INTRODUCTION

Dielectric materials are used in many devices, including capacitors, transistors, transformers, amplifiers, rectifiers, resonators, antennas, wave-guides, and wireless receivers. In this Article, we report independent measurements of an anomalously high dielectric constant ε_r found in dielectric amorphous-oxide (glass) Li^+ or Na^+ electrolytes[1,2] that are being developed as the electrolyte of all-solid-state rechargeable batteries[3,4] that can store electrostatic in addition to electrochemical energy. The combination in a single solid material of a dielectric constant $\varepsilon_r > 10^6$ and a Li^+ or Na^+ conductivity $\sigma_i \geq 10^{-2}$ S cm^{-1} at 25 °C is unique, but the amorphous phase is hygroscopic, and its unique properties depend not only on how it is synthesized but also on how it is conditioned in the amorphous phase.[1]

In the coming era of the Internet of Things (IoT), wireless sensor networks that monitor, detect, and gather data will be vital for advancements in human health, public safety, industrial automation, and energy management, with an expected market of more than a billion dollars by 2025.[5−7] Presently, rechargeable batteries are used to power the wireless network. However, the limitations of today's Li-ion batteries make this power source unfeasible, from both cost and environmental perspectives, for the trillions of sensor nodes predicted to be operating in a few years.[5−7] The dielectric amorphous-oxide Li^+ or Na^+ electrolytes show promise for transforming the rechargeable battery to overcome this obstacle and liberating modern society from its dependence on the energy stored in fossil fuels; the anomalously high ε_r in these materials is a key to this transformation. Here, we report independent measurements of the ε_r in these glasses with experimental and analysis methods different than those used previously; they show that, with optimization of the material properties under a DC electrical field and an appropriate annealing temperature and vacuum relaxation, the extraordinary ε_r of these materials can be significantly enhanced.

A dielectric material is an electronic insulator that can be polarized by an applied electric field E_a; the electric field displaces positive charges in the direction of the field and negative charges in the opposite direction. The polarization in a crystalline material may be the result of (i) a displacement of atomic electronic charge relative to the positive nuclear charge to create a dipolar axis parallel to E_a, (ii) a displacement of cations along a crystal axis from the center of symmetry of their site in an ionically bonded crystal to give a polarization

Received: September 5, 2018
Published: November 27, 2018

DOI: 10.1021/jacs.8b09603
J. Am. Chem. Soc. 2018, 140, 17968−17976

component parallel to E_a, or (iii) an orientation of intrinsically dipolar molecules (e.g., A_2O or OA^-, A = H, Li, and Na) to increase the component of the molecular dipoles parallel to E_a. If the molecular dipoles are also translationally mobile, as may occur in an amorphous solid, the molecular dipoles may interact with one another to form larger ferroelectric linear molecules.[1] In a crystal, the dipoles may not be completely aligned with the direction of E_a. Therefore, polarization in a crystalline material is defined as $P = \chi_o \varepsilon_o E_a$, where ε_o is the permittivity of a vacuum and the susceptibility $\chi_o = \varepsilon_r - 1$ and ε_r are tensors; ε_r is the dielectric constant of the crystal. However, if the solid is amorphous and the permittivity $\varepsilon_r \gg 1$, then χ_o and ε_r become scalar, $\chi_o = \varepsilon_r - 1 \approx \varepsilon_r$, and $P = \varepsilon_o \varepsilon_r E_a$, with an ε_r that varies sensitively with any molecule−dipole orientation and their interactions to form ferroelectric molecules.

Ferroelectric crystals or molecules contain multiple electric dipoles that are cooperatively ordered below a transition temperature T_c. The cooperative ordering below T_c may involve a cooperative creation of the dipoles below a displacive transition at T_c, or it may be an order−disorder transition of existing dipoles. Ferroelectric solids are pyroelectric, and all pyroelectrics are piezoelectrics. This relationship also holds for amorphous solids containing ferroelectric molecules, Figure 1.

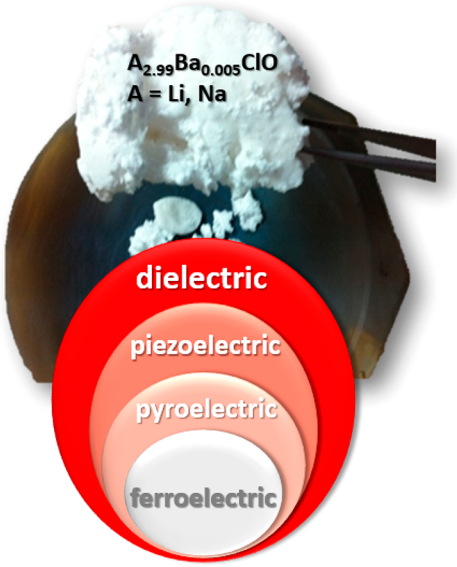

Figure 1. Dielectric, piezoelectric, pyroelectric, and ferroelectric materials and their relationships. As-synthesized morphology of $A_{2.99}Ba_{0.005}ClO$ (A = Li, Na) dielectric electrolyte.

Pyroelectrics generate a voltage in response to being heated or cooled; piezoelectrics become charged and generate a voltage in response to an applied stress. The dielectric glass electrolytes in this study show aging phenomena and hysteresis indicative of the formation of ferroelectric molecules.[1,8]

2. EXPERIMENTAL SECTION

Five-gram samples of Li^+ or Na^+ dielectric amorphous-oxide (glass) electrolytes were synthesized by adding approximately 20 mL of deionized water to 2.3317 g of LiCl, 2.6212 g of Li(OH), and 0.0471 g of $Ba(OH)_2$ precursors of $Li_{2.99}Ba_{0.005}ClO$ and an equal amount of water to 2.1038 g of NaCl, 2.8653 g of Na(OH), and 0.0308 g of $Ba(OH)_2$ precursors of $Na_{2.99}Ba_{0.005}ClO$ (LiOH, Sigma-Aldrich, 98% pure; LiCl, Sigma-Aldrich, ≥99% pure; $Ba(OH)_2$, Sigma-Aldrich, ∼95% pure; Na(OH), Merck, >99.9%; NaCl, Merck, 99.9%). The reagents were added, mixed, and closed in a Teflon reactor that was partially immersed in a sand bath that was heated to 80 °C. After around 2 h, it was verified that the reagents were all well-dissolved. The bath was then slowly heated to 230−240 °C and left at this temperature until all the water evaporated from a loose cap. Evaporation of the water was verified by cooling the reactor until it can be safely opened; a white solid is deposited on the Teflon reactor if the water is all dried out. The reactor with the electrolyte content was then placed in an argon-filled glovebox (H_2O < 0.1 ppm and O_2 < 1 ppm).

The amounts of Li and Ba in the electrolyte were determined with an Agilent 7500ce quadrupole inductively coupled plasma mass spectrometer (ICP-MS). The electron multiplier detection system provides 9 orders of linear dynamic range, from ppt to hundreds of ppm. Since the concentration of the elements for the ICP test should be ≤200 ppm, an adequate amount of electrolyte was weighed (300 mg) so that the concentration of Li and Ba would fall within that range. The samples were digested with 3 mL of HNO_3 (70%, ICP grade) and 3 mL of HCl (32%, ICP grade). Each sample was then heated under a fume hood at 80 °C for 30 min. After cooling, the samples were diluted in 100 mL of H_2O (HPLC grade) and transferred into Falcon test tubes for the ICP test. The Li/Ba ratio obtained corresponded to $Li_{2.993}Ba_{0.007}ClO$. The contents of Cl and O could not be determined by using ICP-MS.

The sample cells were prepared by crushing part of the electrolyte into a fine powder in an Agatha mortar and pestle inside an Ar-filled MBraun glovebox and placing a ca. 1 mm thick layer of the electrolyte powder between two 0.5 mm thick polished solid gold plates of 2.5 × 2.5 cm^2 (Alfa Aesar, 99.999% pure) (Figure S1). The cell was wrapped with Teflon tape carefully applied to avoid short-circuits at the borders. The "sandwich" was then placed in a plastic- or Teflon-wrapped C-clamp. The force used was just enough to hold the powders in contact and did not exceed 700 N.

A Zetasizer Nano ZS dynamic light scattering instrument was used to determine the particle group size of the ground powders before they were pressed with the gold plates. We used absolute ethanol to obtain a colloidal suspension of the particles and determined particle sizes from Brownian thermal motions. The average particle group size obtained was 1.28 μm.

Sample 1: Au/Li^+-Glass/Au. Electrolyte sample 1 was optimized for 2 weeks at ∼170 °C in a furnace in the Au/Li^+-glass/Au cell with the C-clamp prior to starting the measurements. Cyclic voltammetry (CV) measurements (see Figure 2) were performed with a CHI 660D instrument in the Bard laboratory at the University of Texas−Austin.

Sample 2: Au/Na^+-Glass/Au. Electrolyte sample 2 was measured immediately after cell assembly. CV and electrical impedance spectroscopy (EIS) measurements (see Figure 3) were performed with a BioLogic SP240 instrument in the Braga laboratory at the University of Porto. The potential used was 10 mV and the frequencies ranged from 50 mHz to 7 MHz. Equivalent measurements were performed with a CHI 660D instrument in the Bard laboratory at UT-Austin.

Samples 3−5: Au/Li^+-Glass/Au. Electrolyte samples 3−5 were measured immediately after cell assembly. CV and EIS measurements (see Figures 4−6) were performed using a BioLogic VMP300 instrument in the Goodenough laboratory at the Pickle Research Center, UT-Austin. The potential used was 10 mV and the frequencies ranged from 100 mHz to 7 MHz.

3. RESULTS AND DISCUSSION

The dielectric glass electrolytes were shown to contain AO^- and A_2O dipoles (A = Li, Na) that coalesced into chains when studied by *ab initio* molecular dynamics.[1] Previous measurements of the ε_r of the dielectric Li^+- and Na^+-glass electrolytes were obtained from impedance spectroscopy.[1,2,8] At room temperature, these measurements resulted in $10^6 < \varepsilon_r < 10^7$ for the Na^+-glass. Here, we compare ε_r values obtained from both EIS and CV[9] for the Li^+- and Na^+-glasses in three different laboratories. The data were taken at different temperatures with different samples subject to different conditioning.

DOI: 10.1021/jacs.8b09603
J. Am. Chem. Soc. 2018, 140, 17968−17976

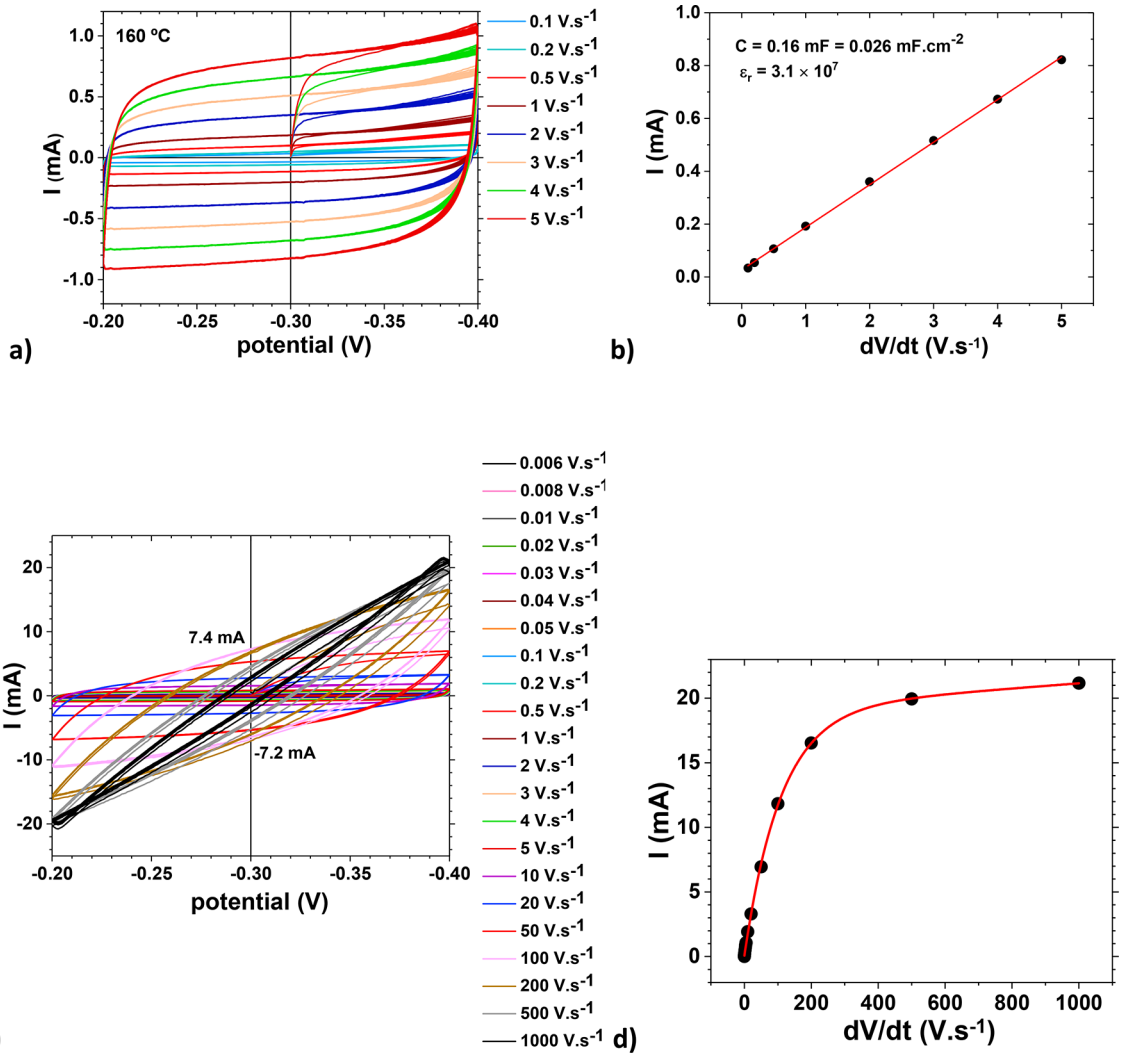

Figure 2. Cyclic voltammetry at 160 °C of a Au/Li^+-glass electrolyte/Au cell with electrolyte sample 1 at different scanning rates of the potential (dV/dt). (a) CV for 0.1−5 V·s^{-1}. (b) Average current at ±0.30 V as a function of the scanning rate (dV/dt) for rates varying from 0.1 to 5 V·s^{-1}. (c) CV for 6 mV·s^{-1} to 1000 V·s^{-1}. (d) Average current at ±0.30 V as a function of the scanning rate (dV/dt) for rates varying from 0.006 to 1000 V·s^{-1}.

Figure 2a shows the CV curves with increasing low sweep rates for sample 1 in a Au/Li^+-glass/Au cell taken at 160 °C; above 140 °C, the electrolyte was dry and amorphous. The glass had been annealed for 2 weeks at 170 °C. The curves show typical capacitive behavior, with the separation of the discharge and charge currents increasing with sweep rate from 0.1 to 5 V·s^{-1}. Since the charge of a capacitor is $Q = CV$ and $I = \frac{dQ}{dt} = \frac{C\,dV}{dt} + \frac{V\,dC}{dt}$, with $0.2 \leq |V| \leq 0.4$ V and $dC/dt \approx 0$ during the interval of time of the experiment, it follows that $\langle I \rangle \approx C\,dV/dt$, where $\langle I \rangle = [I_{disch} + (-I_{ch})]/2$. From the curves of Figure 2a, the $\langle I \rangle_{-0.3}$ vs dV/dt plot of Figure 2b shows a straight line with a slope $C = \varepsilon_0\varepsilon_r A/d$; the ratio A/d of the area to thickness of the electrolyte is measurable and ε_0 is known. The slope of the line in Figure 2b gives $C = 26\ \mu F{\cdot}cm^{-2}$ and thus $\varepsilon_r = 3.1 \times 10^7$ at 160 °C. Figure 2c shows cyclic voltammograms taken at increasing sweep rates from 0.006 to 1000 V·s^{-1}, and Figure 2d shows that the straight-line behavior of Figure 2b holds to $dV/dt \approx 100$ V·s^{-1}. As the sweep rate is increased further to superfast rates, the dipoles are not able to follow the rate of change of voltage, so the slope decreases and, therefore, the capacitance with increasing sweep rate beyond $dV/dt = 100$ V·s^{-1}. Figure 2c,d shows how the slope of $\langle I \rangle_{-0.3}$ vs dV/dt, and consequently C, changes from that at lower sweep rates. A full cycle corresponds to a potential sweep of 0.4 V, which for $dV/dt = 200$ V·s^{-1} corresponds to a frequency of 500 Hz.

Figure 3 shows data for electrolyte sample 2 in a Au/Na^+-glass/Au cell taken at 170 °C. The EIS spectra in Figure 3b gave the ε_r versus frequency curve of Figure 3a, showing a low-frequency value 5.0×10^7 (50 mHz) and $\varepsilon_r \leq 5.7 \times 10^6$ (≥1293 Hz), which is in agreement with the value obtained at high frequencies with the equivalent circuit in Figure 3b (5.2×10^6). The electrolyte sample 1 (Li-glass) and sample 2 (Na-glass) show similar responses to potential frequency and, therefore, electric field frequency. Figure 2c,d shows that, for $dV/dt = 200$ V·s^{-1}, corresponding to $f = 500$ Hz, the capacitance shows an inflection and then starts to decrease markedly, which is also found in Figure 3a for ε_r for approximately the same frequency as expected in dipolar materials.[10] In Figure 3b, $R = R_1 + R_2$, where R_1 is the real impedance at the intersection of the semicircle with the real axis at high frequency and R_2 is the diameter of the semicircle. R_1 is a passive resistance that reflects the resistance of cables, electrodes, electrolyte bulk, and interfaces. R_2 is the resistance to the formation of the electric-double-layer

DOI: 10.1021/jacs.8b09603
J. Am. Chem. Soc. 2018, 140, 17968−17976

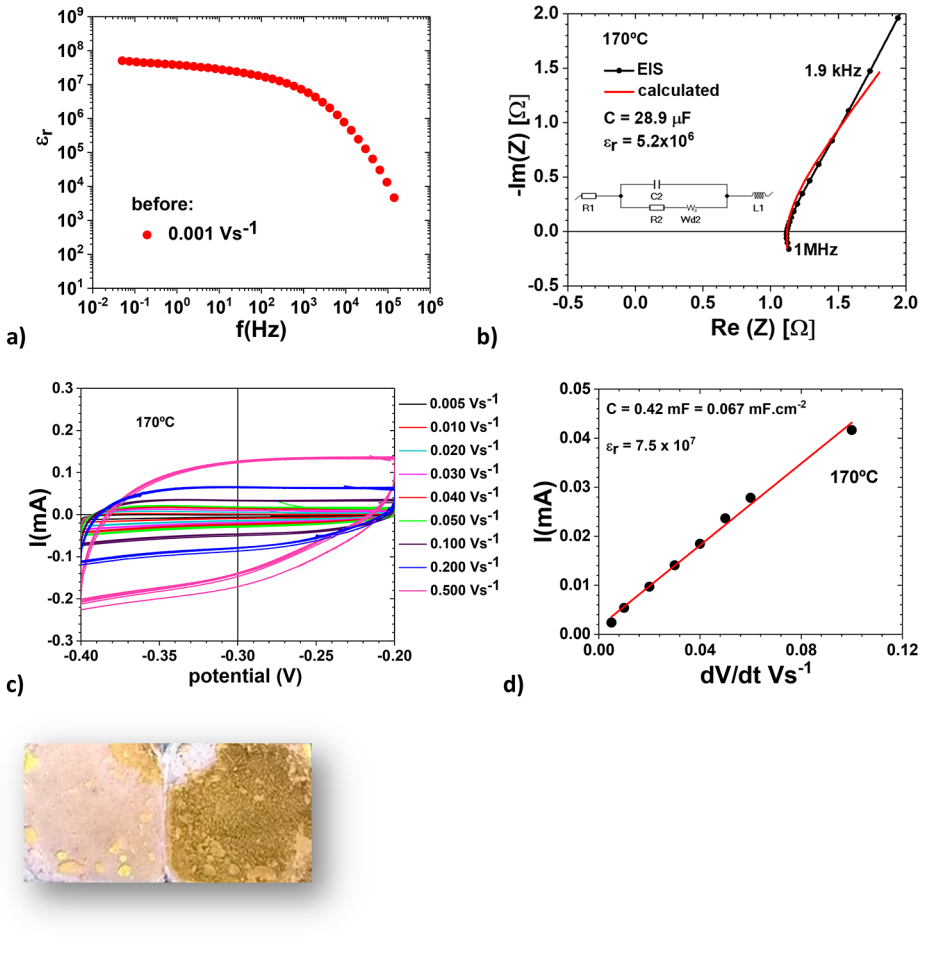

Figure 3. Low- and high-frequency electric impedance spectroscopy (EIS) and cyclic voltammetry (CV) measurements in an Au/Na^+-glass electrolyte/Au cell with electrolyte of sample 2 for determination of the dielectric constant at 170 °C. (a) Dielectric constant vs frequency (low-frequency range). (b) EIS at high frequency and determination of the calculated curve using the equivalent circuit shown in the figure (obtained at 10 mV). (c) CV for sweep rates of the potential (dV/dt) between 0.005 and 0.5 $V{\cdot}s^{-1}$ and (d) the corresponding average of the current at ±0.3 V vs the potential rates (dV/dt) to calculate the capacitance and, subsequently, the dielectric constant. (e) Electrolyte morphology after measurements; most of the electrolyte became a translucent layer (on the left).

capacitors (EDLCs) and reflects the resistance of the electrolyte. The Warburg element Wd_2 of the equivalent circuit in Figure 3b (straight line with constant phase of 45°) reflects the resistance of the electrolyte diffusive layer associated with the EDLC.[11] L_1 is the inductance (positive impedance) due to the time-variable magnetic flux generated in the cables that, at high frequencies and high capacitances is particularly important and unavoidable, in accordance with Faraday's induction law. The capacitance C = 28.9 μF is obtained from the maximum of the semicircle, which corresponds to $\omega_\tau = 1$, where τ is the capacitor's time constant and $\omega = 2\pi f = (R_2C_2)^{-1}$. The cell was then subjected to CV, Figure 3c. As in Figure 2b, the $\langle I \rangle$ vs dV/dt of Figure 3d shows a straight line and capacitance C from which an $\varepsilon_r = 7.5 \times 10^7$ was obtained in good agreement with the low-frequency ε_r obtained with impedance spectroscopy ($\varepsilon_r = 5.0 \times 10^7$ at 50 mHz). The morphology of the Na^+-glass after the experiment is shown in Figure 3e; the electrolyte became semi-transparent. While no Faradaic interactions are expected to have occurred in the experiments of Figures 2 and 3, highlighting a pure capacitive behavior; in the subsequent experiments between −10 and +10 V, minor faradaic interactions might have occurred even though not observed.

The polarization is $P = (Q - Q_0)/A = \varepsilon_0\varepsilon_r E_a$, where $Q - Q_0$ is the variation of the charge as a result of the applied electrical field $E_a = \Delta V/d$, which corresponds to $\Delta Q = C\Delta V$, since the capacitance $C = \varepsilon_0\varepsilon_r A/d$ as defined for a parallel-plate capacitor in accordance with Gauss's law. Figure 4a,b shows the variation of the polarization of sample 3 in a Au/Li^+-glass/Au cell at 140 °C with a CV taken at 0.05 $V{\cdot}s^{-1}$ vs the applied electric field and cycle number. The polarization increased with cycle number for the first 50 cycles, but then showed a tendency to increase more slowly, evidencing that the cell performance was close to being optimized. Figure 4c shows the CV corresponding to Figure 4a,b, and from $\langle I \rangle$ between $-2.1 < V(V) < 2.1$, the permittivity $\varepsilon_r = 5.7 \times 10^7$, calculated at 0 V, was obtained. Figure 4d shows the CV for the same sample 3 taken at 25 °C after 1 week of relaxation under a vacuum at room temperature subsequent to the experiment in Figure 4a−c; the obtained $\varepsilon_r = 6.9 \times 10^9$, calculated at 0 V had increased 2 orders of magnitude in that time. Figure 4e shows the current, potential and total charge versus time for a full cycle from −10 to +10 V. The charge versus potential is shown in Figure 4f; it is observed that the two electrodes developed some inequality after the second cycle. The latter is not as evident in Figure 4g with the Au/Li^+-glass/Au cell at 220 °C. Figure 4g shows negative differential

DOI: 10.1021/jacs.8b09603
J. Am. Chem. Soc. 2018, 140, 17968−17976

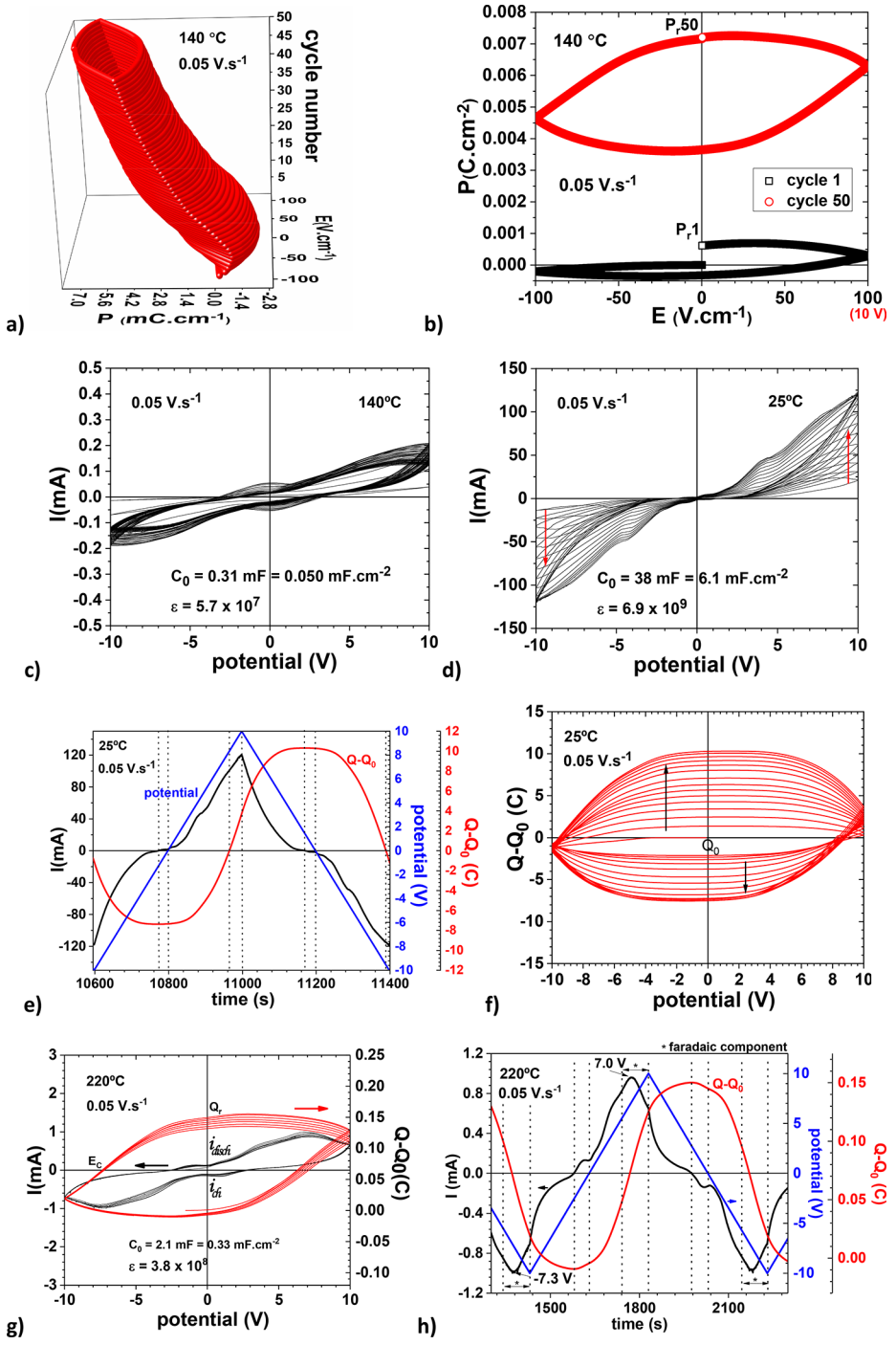

Figure 4. Cyclic voltammetry for two different electrolyte samples, 3 and 4, in an Au/Li^+-glass electrolyte/Au cell. (a) 3D graph of the polarization as a function of the electric field and cycle number for sample 3, highlighting how the polarization changes so perceptibly with cycle number at 140 °C. (b) Polarization vs electric field showing the polarization difference between cycles 1 and 50 of experiment (a). (c) CV corresponding to (a) and (b), current vs potential. (d) CV at 25 °C for sample 3 after one week of relaxation under a vacuum, showing a 2 orders of magnitude increase in the dielectric constant in spite of the less favorable experimental temperature. (e) Detail of current and total charge vs time from (d), showing discharge of one physical capacitor and three capacitances from −10 to +10 V and corresponding charge from +10 to −10 V. (f) Total charge vs potential for experiment (d), showing a certain inequality between electrodes after the second cycle. (g) CV and total charge as a function of potential at 220 °C for sample 4 which was synthesized at the same time as sample 3 but had an extra round of cycles and one night of relaxation under a vacuum, Q_R is the remanent polarization and E_C the coercive electric field, (h) Current and total charge vs time from (g), showing discharge of one physical capacitor and three capacitances from −10 to +10 V and corresponding charge from +10 to −10 V superimposed with faradaic interaction from −7.3 to −10 V and from +5.5 to +10 V.

resistance,[12] $R_{diff} = dV/dI$, from −7.5 to −10 V (−9.0 kΩ) and from +7.1 to +10 V (−8.9 kΩ). This negative resistance results from a faradaic interaction on one of the electrodes leading to the formation of a product layer. In the experiment of Figure 4g, the Faradaic interaction seems to have been initiated at ±5.5 V, the potential at which it starts to deviate from capacitive

DOI: 10.1021/jacs.8b09603
J. Am. Chem. Soc. 2018, 140, 17968−17976

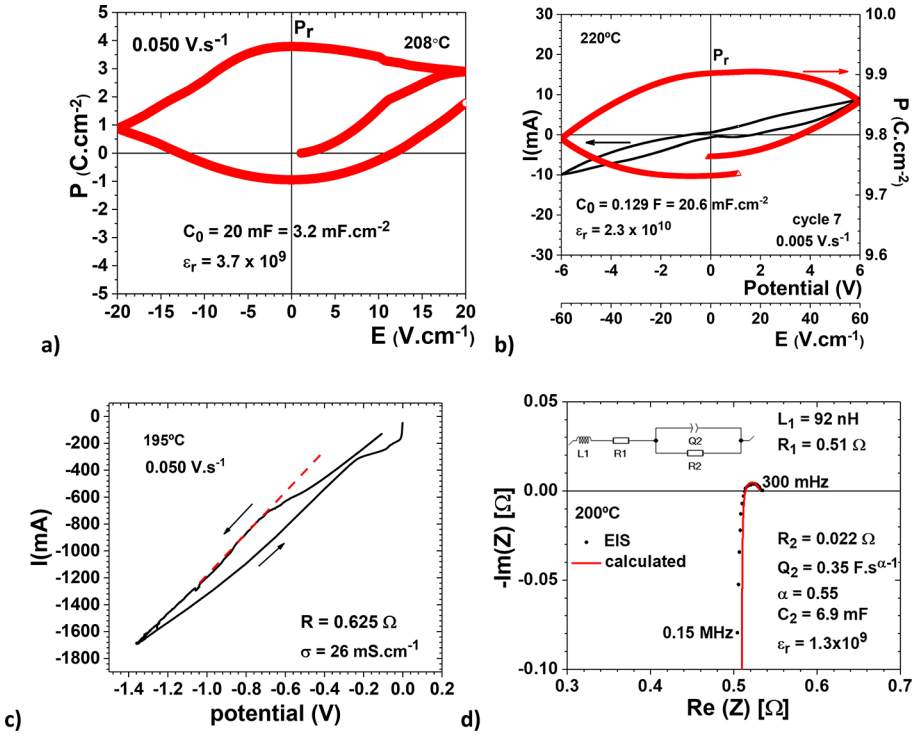

Figure 5. Total polarization vs electric field, CV, and EIS for sample 5 in a Au/Li^+-glass electrolyte/Au cell. (a) Polarization vs electric field at 208 °C after 2 rounds of cycles and 1 night relaxation under a vacuum. (b) CV and polarization vs electric field at 220 °C after three rounds of cycles and two nights of relaxation under a vacuum. (c) CV at 195 °C after three rounds of cycles and two nights of relaxation under a vacuum and calculation of the resistance to capacitor formation by calculating the V vs I slope and applying Ohm's law. (d) EIS at 200 °C after three rounds of cycles and two nights of relaxation under a vacuum showing results for the resistance comparable to the resistance calculated after (c) and capacitance comparable to that calculated in (b) taking into consideration the different methods and temperature difference.

behavior as shown in Figure 4h. The differential negative resistance corresponding to an increase in voltage takes place when reaching a critical thickness of the product layer at which the Fermi level of the electrode step-changes to the Fermi level of the product layer, resulting in an "on/off" increase/decrease of the charge accumulated at the interfaces to align the new electrolyte/electrode Fermi levels.

The polarizations are nearly constant in the range $-2 \le V\,(\mathrm{V}) \le 2$ $(-20 \le E\ (\mathrm{V{\cdot}cm^{-1}}) \le 20)$ once a steady equilibrium is achieved, as observed in Figure 5a,b. The optimization and slightly higher temperature are reflected in an approximately 1 order of magnitude increase in the relative permittivity (from $\varepsilon_r = 3.7 \times 10^9$ in Figure 5a to $\varepsilon_r = 2.3 \times 10^{10}$ in Figure 5b). The resistance to formation of the EDLC in the capacitor, obtained from the slope of the I versus V line of Figure 5c $(1/R = \mathrm{d}I/\mathrm{d}V)$, shows a conductivity of about 26 $\mathrm{mS{\cdot}cm^{-1}}$ for a sweep rate of 0.050 $\mathrm{V{\cdot}s^{-1}}$. In the EIS spectrum in Figure 5d, the impedance of the constant phase element Q_2 in the equivalent circuit in Figure 5d can be related to the capacitance $C = (QR)^{1/\alpha}/R$, where R is the resistance to the formation of the capacitor and $0 < \alpha \le 1$, $C_2 = 6.9$ mF is used to calculate the permittivity, $\varepsilon_r = 1.3 \times 10^9$ (high frequency) at 200 °C, and $\varepsilon_r \simeq 2.3 \times 10^{10}$ (low frequency) is obtained from the CV curve in the interval $-2.0 \le V\,(\mathrm{V}) \le 2.0$ for this optimized Au/Li^+-glass/Au cell. The permittivity decreases rapidly with frequency for $f \gtrsim 500$ Hz; the resistance seems to decrease as well (0.625 Ω at $f \approx 10$ mHz and 0.022 Ω at $f \gtrsim 300$ mHz).

It is important to highlight that Figures 4b,f,g and 5b clearly show negative differential capacitance for $3 < V\,(\mathrm{V}) < 10$ and $-10 < V\,(\mathrm{V}) < -3$, $C_{\mathrm{diff}} = \frac{\mathrm{d}Q}{\mathrm{d}V} = \left(\frac{\mathrm{d}^2U}{\mathrm{d}Q^2}\right)^{-1}$, where U is the potential energy, which is characteristic of a field effect transistor with ferroelectric oxides that can make a conventional field effect transistor have super-steep switching characteristics of sub-threshold slope;[12] the study of negative capacitance field effect transistors started in 2008[13−15] and has been receiving increasing interest as a solution to overcome Moore's law.[12] We highlight that, in Figure 4g, the negative differential capacitance (see Figure S2)[16] is partially canceled by the faradaic interaction since the reduction reaction taking place at the electrode/electrolyte interface reduces the electrolytes' polarization.

Figure 6 provides our model and interpretation of the change with applied voltage of the current, polarization, and capacitance values and the changing resistance to the EDLC formation at different potentials. For additional information on the variation of the electrochemical potentials upon contact in hetero-junctions, see ref 17.

Outside the cells, the electrochemical potential (Fermi level) of gold is $\mu_{\mathrm{Au}} = -5.9$ eV, referenced to vacuum (0 eV), and the Fermi level of the Li^+-glass electrolyte is $\mu_{\mathrm{electrolyte}} = -3.8$ eV. The glass electrolyte oxide has a Fermi level (electrochemical potential) given by $\mu = -(\mathrm{IP} + \mathrm{EA})/2$, where IP is the ionization potential and EA is the electron affinity, which in an insulator amorphous material is defined as the energy level at the middle of the energy gap between the bottom of the conduction states and the top of the valence states.[18] The exact definition is $\mu = (\partial E/\partial N)_Z$, where E is the potential energy, N is the number of electrons and Z is the potential due to the nuclei, plus any external potential.[18−20]

In our cells, the Au/electrolyte interfaces are heterojunctions, and the force to equalize the Fermi levels at an interface creates

DOI: 10.1021/jacs.8b09603
J. Am. Chem. Soc. 2018, 140, 17968−17976

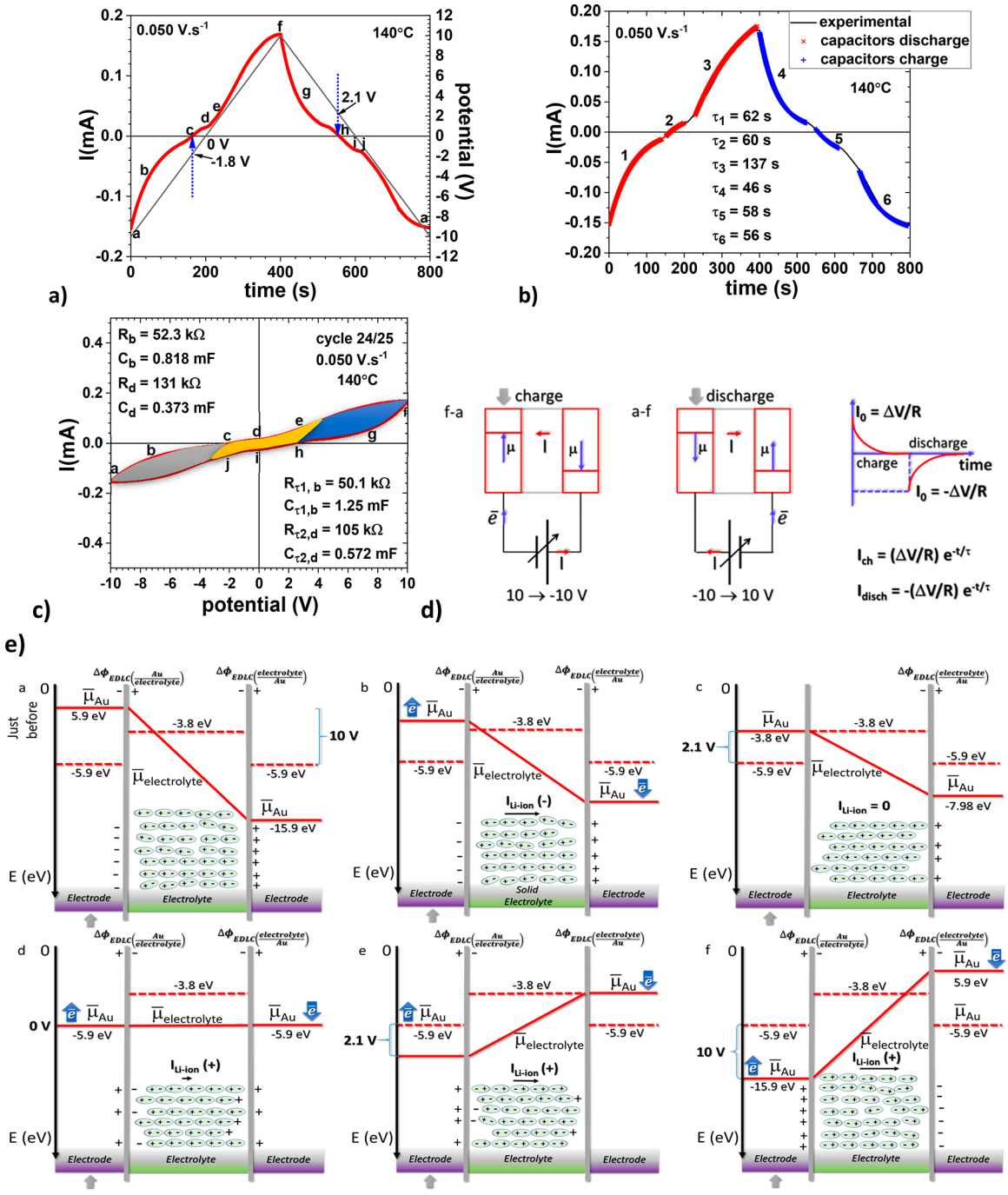

Figure 6. Current vs time for sample 3 of Figure 4a–c and model of the Fermi level variations vs the applied potential in a CV experiment. (a) Discharge and charge of three different capacitances corresponding to one physical capacitor and key points: a-b-c first, c-d-e second, and e-f third discharging capacitances, and f-g-h first, h-i-j second, and j-a third charging capacitances. (b) Experimental and fitted discharge/charge of the capacitor in (a), as well as corresponding capacitor time constants. (c) CV for part of cycles 24 and 25 of Figure 4c, highlighting important landmarks of (a) and of the variation of Fermi level models as well as capacitances and resistances obtained directly from the CV (with $\frac{i_{disch} + (-i_{ch})}{2} = C\frac{dV}{dt}$ and $\frac{1}{slope} = 1/R$, respectively) and from the fitting of the discharge equations for a capacitor, Table 1. The shaded areas correspond to the three capacitances for one physical capacitor, which in fact should only be one in ideal conditions. (d) Schematic variation of the electrochemical potentials of gold electrodes and current during charge and discharge in a CV measurement. (e) Variation of the relative Fermi levels, current, and electrolyte polarization showing the three capacitances shown experimentally during discharge: first a-b-c (electrode polarizations: negative (WE)/positive), second c-d-e (electrode polarizations: positive (WE)/positive), and third e-f (electrode polarizations: positive (WE)/negative). The arrows in (d) and (e) indicate the working electrode (WE).

an EDLC at each electrode/electrolyte interface. The EDLCs formed at the electrolyte interfaces shift the electrolyte Fermi level to the same lower energy as the gold since the electrolyte possesses free cations that can move away from a surface, leaving negatively charged Li^+ vacancies behind. Slower-moving electric dipoles that condense into ferroelectric molecules also contribute over time to the charge of the EDLCs and to the polarization of the electrolyte. These slower-moving electric

DOI: 10.1021/jacs.8b09603
J. Am. Chem. Soc. 2018, 140, 17968–17976

dipoles are responsible for the aging phenomenon that was observed.

The metal accumulates mirror electronic holes at the Au surfaces with the electrolyte. Moreover, the gold does not change its Fermi level much since no electrons are exchanged with the electrolyte where no Faradaic reactions take place; the open-circuit voltage of the Au/Li^+-glass/Au cell remains $V_{oc} = 0$ V (Figure S2).

Figure 6a,b shows that the CV curves can be interpreted as reflecting the charge/discharge of capacitors, which had been defined above in Figure 4c,d. Each of the three sub-parts of the I vs time curve observed in the potential ranges from −10 to +10 V or +10 to −10 V of Figures 6a−c can be interpreted as the discharge/charge curve of a different unitary capacitor, defined by its capacitance C, with a dielectric of thickness d and a surface area A corresponding to the thickness and surface area of the cell. All the latter capacitors are the same equivalent capacitor. The two EDLCs formed at each interface are not independent because they are connected by the aligned dipoles in the ferroelectric material; the entire electrolyte, including the two EDLCs, can, therefore, be considered a simple capacitor instead of two EDLCs in series (see Figures 6b and S3, and Table 1).

Table 1. Discharge/Charge Equations and Parameters for the Six Different Capacitances Corresponding to the Same Physical Capacitor, Resulting from the Corresponding Curve Fittings at 140 and 25 °C

discharge (140 °C)			discharge (25 °C)		
	$I_{disch} = I_i - I_0 e^{-t/\tau}$	$I_0 = \Delta V/R$, $\tau = RC$		$I_{disch} = I_i - I_0 e^{-t/\tau}$	$I_0 = \Delta V/R$, $\tau = RC$
region	I_i (mA), I_0 (mA), τ (s)	ΔV (V), R (Ω), C (F)	region	I_i (mA), I_0 (mA), τ (s)	ΔV (V), R (Ω), C (F)
1	0.00494, 0.158, 62.4	7.9, 50.1 × 10^3, 1.25 × 10^{-3}	1	10.9, 131, 68.1	7.9, 60.1, 1.13
2	0.0329, 0.0399, 60.3	4.2, 105 × 10^3, 0.572 × 10^{-3}	2	79.4, 63.7, 58.0	4.2, 66.0, 0.879
3	0.238, 0.211, 137	7.9, 37.5 × 10^3, 3.65 × 10^{-3}	3	207, 151, 166	7.9, 52.2, 3.18
charge (140 °C)			charge (25 °C)		
	$I_{ch} = I_i + I_0 e^{-t/\tau}$	$I_0 = \Delta V/R$, $\tau = RC$		$I_{ch} = I_i + I_0 e^{-t/\tau}$	$I_0 = \Delta V/R$, $\tau = RC$
region	I_i (mA), I_0 (mA), τ (s)	ΔV (V), R (Ω), C (F)	region	I_i (mA), I_0 (mA), τ (s)	ΔV (V), R (Ω), C (F)
4	0.00485, 0.160, 46.0	7.9, 49.3 × 10^3, 0.932 × 10^{-3}	4	−13.5, 140, 71.9	7.9, 56.5, 1.27
5	−0.0427, 0.0475, 57.7	4.2, 88.5 × 10^3, 0.653 × 10^{-3}	5	−92.2, 79.6, 70.6	4.2, 52.8, 1.34
6	−0.165, 0.100, 55.5	7.9, 78.8 × 10^3, 0.704 × 10^{-3}	6	−147, 87.6, 79.5	7.9, 90.2, 0.882

The capacitor being charged or discharged depends on which electrode is considered the working electrode (WE) and what is the initial polarization, as schematized in Figure 6d. In Figure 6b, we choose the WE as the initial negative electrode; the capacitors are being discharged in regions 1−3 and charged in regions 4−6 (see Table 1 and Figure S3 for similar analysis at 25 °C). In the interval a−c, (region 1), the capacitor discharges (WE is negative, current $I(-)$) and the polarization increases in absolute value (see Figure 4e for visualizing the variation of the polarization at 25 °C). In c−e (region 2), the capacitor discharges (WE becomes positive, current $I(+)$) and the polarization flattens out. In e-f (region 3), the capacitor discharges (WE is positive, current $I(+)$) and the polarization slowly decreases in absolute value. In the interval f-h (region 4), the capacitor charges (WE is positive, current $I(+)$) and the polarization slowly increases in absolute value. In h-j (region 5), the capacitor charges (WE becomes negative, current $I(-)$) and the polarization flattens out. Finally, in j-a (region 6), the capacitor charges (WE is negative, current $I(-)$) and the polarization slowly decreases in absolute value. We highlight in Figure 6c the three slightly different capacitances represented by shaded areas, which in ideal conditions are just one capacitance. The results in Table 1 are in agreement with the latter observation.

From −10 to −2.1 V, Figure 6e schematics a−c, the direction of the current is negative because the WE (discharging electrode) is negative, and an electric field inside the electrolyte develops a polarization field in opposition to the internal field to reduce the electric field inside the electrolyte. This change is reflected in the change of slope of the CV curves (capacitor resistance) and the increase of the polarization in absolute value. At −2.1 V, Figure 6e schematic c, the cell is at $I = 0$ (infinite resistance) during an instant when the Fermi levels between the WE and the electrolyte are equal, which suppresses the formation of an EDLC.

In the voltage range $-2.1 \le V\,(\mathrm{V}) \le 2.1$, Figure 6e, schematics c−e, an applied potential changes the charge of the two EDLCs but not the direction of their electric field. Although the applied current resulting from the applied potential remains in the same direction, the WE becomes positive at $V > -2.1$ V and so does the current $I(+)$. The WE (discharging electrode Figure 6d) remains positive from +2.1 to +10 V. At an applied voltage $V = 0$ V, two similar EDLCs are formed by a similar movement of the mobile cations in the electrolyte away from each interface to create a positive charge within the electrolyte and a negative charge in the electrode at each interface. This ionic motion leaves no electric field inside the cell to reorient the electric dipoles. The polarization flattens out since the electrolyte is a ferroelectric material (Figure 6e schematic d) and, consequently, holds its polarization even in the absence of an electric field. Thus, we determine the intrinsic ε_r from the voltage range $-2.1 \le V\,(\mathrm{V}) \le +2.1$ in the CV profile.

From +2.1 to +10 V, the electric field inside the electrolyte is opposite to the electric field from −10 to −2.1 V and the polarization slowly decreases in absolute value, Figure 6e schematic f.

It is worth highlighting that any Faradaic reactions, like those observed in Figure 4g,h, that might occur at the WE from −10 to −2.1 V should lead to the formation of a Au−Li alloy (the EDLC at the interface is formed by electrons on the Au surface and Li^+ in the electrolyte), while between −2.1 and +10 V the formation of $AuCl_3$ and AuCl[21−24] salts may occur (the EDLC at the interface is formed by Au^{3+} and Au^+ and Li^+ vacancies rich in chlorine). Water converts AuCl to a mixture of Au and $AuCl_3$, which is a citron-yellow amorphous powder.[24] We dried the electrolyte well inside the glovebox before experiments above 140 °C outside the glovebox. The formation of AuCl takes place at ±0.6 V and is reversible.[22] The reduced AuCl at the surface is almost black.[22]

DOI: 10.1021/jacs.8b09603
J. Am. Chem. Soc. 2018, 140, 17968−17976

4. CONCLUSIONS

In summary, we have demonstrated that the dielectric amorphous-oxide (glass) electrolyte exhibits anomalously large dielectric constants that can reach values of $\varepsilon_r \approx 7 \times 10^9$ at 25 °C and values in excess of 10^{10} at 220 °C after optimization of the electrolyte by cycling in a Au/A^+-glass/Au cell with A = Li or Na. The Na^+ electrolytes can have a somewhat higher ε_r than the Li^+ electrolytes. These extraordinarily high dielectric constants make these glasses of potential interest for a range of electrical devices as well as for rechargeable batteries that can power not only electric vehicles and the grid but also, in a few years, the trillions of nodes of the wireless Internet of Things by taking advantage of the ferroelectric character of the electrolyte, which allows electrostatic in addition to electrochemical storage that can increase substantially the capacity of the devices. Conditioning of the glass involves interactions between intrinsic A_2O and AO^- (A = Li, Na) electric dipoles to form linear ferroelectric molecules aligned by the internal electric field; the ferroelectric molecules release mobile A^+ cations responsible for the high cation conductivities σ_i that, with ε_r, increase with temperature. However, the glass electrolytes are hygroscopic and, therefore, need to be handled appropriately.

A new model relating the CV of a ferroelectric material between gold electrodes to the variation of the electrochemical potentials of the materials in contact is presented, paving the way to a universal model.

■ ASSOCIATED CONTENT

Supporting Information

The Supporting Information is available free of charge on the ACS Publications website at DOI: 10.1021/jacs.8b09603.

Au/Li^+-glass electrolyte/Au cells' photos and thicknesses, capacitors and Fermi levels schematics, and additional CV cycles, including Figures S1−S4 (PDF)

■ AUTHOR INFORMATION

Corresponding Authors

*mbraga@fe.up.pt

*jgoodenough@mail.utexas.edu

ORCID

Tianhan Kai: 0000-0001-5667-1426

Allen J. Bard: 0000-0002-8517-0230

John B. Goodenough: 0000-0001-9350-3034

Notes

The authors declare no competing financial interest.

■ ACKNOWLEDGMENTS

This work is the product of a collaborative research project between the University of Porto, Portugal, and The University of Texas at Austin. We are thankful to Dr. S. Kalami for performing the ICP-MS tests. M.H.B. and J.E.O. acknowledge the COMPETE2020 and FCT project, EU and Portugal, PTDC/CTM-ENE/2391/2014.

■ REFERENCES

(1) Braga, M. H.; Ferreira, J. A.; Murchison, A. J.; Goodenough, J. B. Electric Dipoles and Ionic Conductivity in a Na^+ Glass Electrolyte. *J. Electrochem. Soc.* **2017**, *164* (2), A207−A213.

(2) Braga, M. H.; Murchison, A. J.; Ferreira, J. A.; Singh, P.; Goodenough, J. B. Glass-Amorphous Alkali-Ion Solid Electrolytes and Their Performance in Symmetrical Cells. *Energy Environ. Sci.* **2016**, *9* (3), 948−954.

(3) Braga, M. H.; Grundish, N. S.; Murchison, A. J.; Goodenough, J. B. Alternative Strategy for a Safe Rechargeable Battery. *Energy Environ. Sci.* **2017**, *10*, 331−336.

(4) Braga, M. H.; Subramaniyam, C. M.; Murchison, A. J.; Goodenough, J. B. Nontraditional, Safe, High Voltage Rechargeable Cells of Long Cycle Life. *J. Am. Chem. Soc.* **2018**, *140* (20), 6343−6352.

(5) Shirvanimoghaddam, M.; Shirvanimoghaddam, K.; Abolhasani, M. M.; Farhangi, M.; Barsari, V. Z.; Liu, H.; Dohler, M.; Naebe, M. Paving the Path to a Green and Self-Powered Internet of Things, *arXiv.org*, 2017; https://arxiv.org/abs/1712.02277 (accessed August 7, 2018)

(6) Narita, F.; Fox, M. A Review on Piezoelectric, Magnetostrictive, and Magnetoelectric Materials and Device. *Adv. Eng. Mater.* **2018**, *20* (5), 1700743.

(7) Wu, W.; Wang, Z. L. Piezotronics and piezo-phototronics for adaptive electronics and optoelectronics. *Nat. Rev. Mater.* **2016**, *1*, 16031.

(8) Braga, M. H.; Stockhausen, V.; Ferreira, J. A.; Oliveira, J. C. E.; El-Azab, A. Novel Li3ClO Based Glasses with Superionic Properties for Lithium Batteries. *J. Mater. Chem. A* **2014**, *2*, 5470−5480.

(9) Bard, A. J.; Faulkner, L. R. *Electrochemical Methods: Fundamentals and Applications*, 2nd ed.; J. Wiley & Sons, Inc., 2001.

(10) Kittel, C. *Introduction to Solid State Physics*, 8th ed.; Wiley, 2005.

(11) Mei, B. M.; Munteshari, O.; Lau, J.; Dunn, B.; Pilon, L. Physical Interpretations of Nyquist Plots for EDLC Electrodes and Devices. *J. Phys. Chem. C* **2018**, *122* (1), 194−206.

(12) Ko, E.; Shin, J.; Shin, C. Steep switching devices for low power applications: negative differential capacitance/resistance field effect transistors. *Nano Convergence* **2018**, *5*, 2.

(13) Khan, A. I.; Chatterjee, K.; Wang, B.; Drapcho, S.; You, L.; Serrao, C.; Bakaul, S. R.; Ramesh, R.; Salahuddin, S. Negative Capacitance in a Ferroelectric Capacitor. *Nat. Mater.* **2015**, *14*, 182−186.

(14) Salahuddin, S.; Datta, S. Use of Negative Capacitance to Provide Voltage Amplification for Low Power Nanoscale Devices. *Nano Lett.* **2008**, *8* (2), 405−410.

(15) Catalan, G.; Jiménez, D.; Gruverman, A. Negative capacitance detected. *Nat. Mater.* **2015**, *14*, 137−139.

(16) Alam, A. A Tutorial Introduction to Negative Capacitor Field Effect Transistors: Perspective on The Road Ahead, 2015; https://nanohub.org/resources/23171/download/2015.12.03-Alam-NEEDS.pdf (accessed Aug 7, 2018).

(17) Braga, M. H.; Grundish, N. S.; Murchison, A. J.; Goodenough, J. B. Thermodynamic considerations of same-metal electrodes in an asymmetric cell. *Materials Theory* **2018**, in press.

(18) Walsh, A.; Butler, K. T. Prediction of Electron Energies in Metal Oxides. *Acc. Chem. Res.* **2014**, *47* (2), 364−372.

(19) Mulliken, R. S. A new electroaffinity scale; together with data on valence states and on valence ionization potentials and electron affinities. *J. Chem. Phys.* **1934**, *2*, 782−793.

(20) Pearson, R. G. Absolute electronegativity and hardness: Application to inorganic chemistry. *Inorg. Chem.* **1988**, *27*, 734−740.

(21) Hofman, H. O.; Magnuson, M. G. The effect of silver on the chlorination and bromination of gold. *Trans. Am. Inst. Mining Eng.* **1904**, 421−433.

(22) Ballantyne, A. D.; Forrest, G. C. H.; Frisch, G.; Hartley, J. M.; Ryder, K. S. Electrochemistry and speciation of Au+ in a deep eutectic solvent: growth and morphology of galvanic immersion coatings. *Phys. Chem. Chem. Phys.* **2015**, *17*, 30540.

(23) Uehara, A.; Chang, S.-Y.; Booth, S. G.; Schroeder, S. L. M.; Mosselmans, J. F. W.; Dryfe, R. A. W. Redox and Ligand Exchange during the Reaction of Tetrachloroaurate with Hexacyanoferrate(II) at a Liquid-Liquid Interface: Voltammetry and X-ray Absorption Fine-Structure Studies. *Electrochim. Acta* **2016**, *190*, 997−1006.

(24) Michaud, L. D., https://www.911metallurgist.com/blog/gold-chloride, Oct 24, 2016 (accessed July 25, 2018).